LETTER

nature cell biology

EB1 interacts with outwardly curved and straight regions of the microtubule lattice

Audrey Guesdon[1,7], Franck Bazile[1,7], Rubén M. Buey[2,3], Renu Mohan[4], Solange Monier[1], Ruddi Rodríguez García[4], Morgane Angevin[1], Claire Heichette[1], Ralph Wieneke[5], Robert Tampé[5], Laurence Duchesne[1], Anna Akhmanova[4], Michel O. Steinmetz[2,8] and Denis Chrétien[1,6,8]

EB1 is a microtubule plus-end tracking protein that recognizes GTP-tubulin dimers in microtubules[1–4] and thus represents a unique probe to investigate the architecture of the GTP cap of growing microtubule ends[5,6]. Here, we conjugated EB1 to gold nanoparticles (EB1-gold) and imaged by cryo-electron tomography its interaction with dynamic microtubules assembled *in vitro* from purified tubulin. EB1-gold forms comets at the ends of microtubules assembled in the presence of GTP, and interacts with the outer surface of curved and straight tubulin sheets as well as closed regions of the microtubule lattice. Microtubules assembled in the presence of GTP, different GTP analogues or cell extracts display similarly curved sheets at their growing ends, which gradually straighten as their protofilament number increases until they close into a tube. Together, our data provide unique structural information on the interaction of EB1 with growing microtubule ends. They further offer insights into the conformational changes that tubulin dimers undergo during microtubule assembly and the architecture of the GTP-cap region.

The spatial and temporal organization of microtubules and their interactions with cellular targets are precisely regulated by an ensemble of stabilizing and destabilizing proteins[7]. Yet, the ability to switch stochastically between growing and shrinking phases is intrinsic to microtubules assembled from purified tubulin[8]. This behaviour, termed 'dynamic instability', is fuelled by the hydrolysis of the GTP nucleotide bound to the β-subunit of the αβ-tubulin heterodimer, which occurs during microtubule assembly. GTP hydrolysis and/or P_i release are supposed to be delayed with respect to tubulin polymerization, giving rise to a protecting layer of GTP- and/or GDP-P_i-tubulin dimers at growing microtubule ends, the so-called 'GTP-cap'[9,10]. However, both the structure of this capping region and the conformational changes that tubulin dimers undergo in the growing microtubule end region during assembly have remained elusive, primarily due to the lack of suitable probes that can visualize the GTP-cap at the single-molecule level.

Recent studies showed that end-binding proteins (EBs) bind with high affinity to the shaft of microtubules assembled in the presence of GTP/GDP-P_i analogues[1,2], suggesting that they recognize the terminal GTP-cap region of growing microtubule ends. In this study, we aimed to characterize the architecture of the end-binding region of EB1 at molecular resolution by cryo-electron tomography (CET) to obtain insights into the GTP cap of growing microtubule ends. Since EB1 is too small to be directly visualized by CET, we conjugated the molecule to gold nanoparticles (NPs) at a controlled stoichiometric ratio[11]. To this end, we incorporated a 6xHis-tag into a loop region of the carboxy-terminal cargo-binding domain of EB1, which is located remote from its microtubule-binding domain (EB1-HisLoop; Supplementary Fig. 1a). To conjugate EB1-HisLoop with NPs, we coated commercial 5- and 10-nm-diameter NPs with a mixed HS-PEG-peptidol matrix[12] that was functionalized with Ni-trisNTA groups[13]. The size distributions of both types of NP were analysed by transmission electron microscopy, providing average diameters of 6.5 ± 1.1 nm and 9.8 ± 0.9 nm, respectively (6.5 and 9.8 nm NPs, Supplementary Fig. 1b). Conjugation of EB1-HisLoop with NPs (EB1-gold) was performed in the presence of a large excess of the protein, and its efficiency was estimated by SDS–PAGE (Supplementary Fig. 1c,d). Densitometry of the Coomassie-stained gels revealed an EB1-monomer/NP molar ratio of about 0.8:1, suggesting that most NPs were effectively conjugated to the EB1-HisLoop molecules. No detectable amount of EB1-HisLoop was found after incubation with non-functionalized NPs and extensive

[1]Institute of Genetics and Development of Rennes, UMR6290 CNRS, University of Rennes 1, Campus Universitaire de Beaulieu, 35042 Rennes Cédex, France. [2]Laboratory of Biomolecular Research, Department of Biology and Chemistry, Paul Scherrer Institut, CH-5232 Villigen PSI, Switzerland. [3]Metabolic Engineering Group, Department of Microbiology and Genetics, University of Salamanca, Campus Miguel de Unamuno s/n, 37007 Salamanca, Spain. [4]Cell Biology, Faculty of Science, Utrecht University, Padualaan 8, 3584 CH Utrecht, The Netherlands. [5]Institute of Biochemistry, Biocenter, and Cluster of Excellence-Macromolecular Complexes, Goethe-University Frankfurt, Max-von-Laue Strasse 9, 60438 Frankfurt am Main, Germany. [6]Microscopy Rennes Imaging Centre, and Biosit, UMS3480 CNRS, University of Rennes 1, Campus Santé de Villejean, 35043 Rennes Cédex, France. [7]These authors contributed equally to this work.
[8]Correspondence should be addressed to M.O.S or D.C. (e-mail: michel.steinmetz@psi.ch or denis.chretien@univ-rennes1.fr)

Received 9 September 2015; accepted 18 August 2016; published online 12 September 2016; DOI: 10.1038/ncb3412

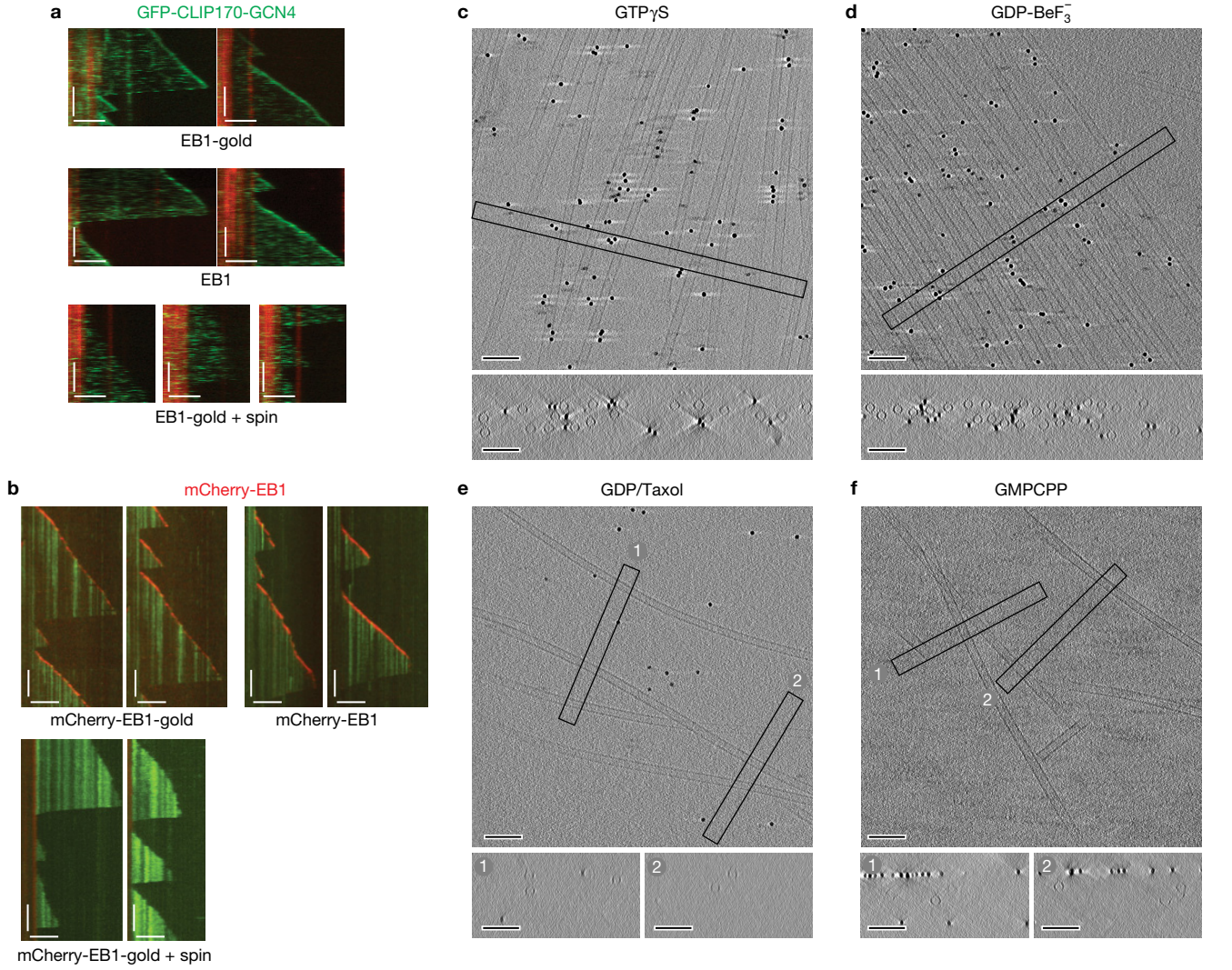

Figure 1 Functional characterization of EB1-gold. (**a**) Recruitment of GFP-CLIP170-GCN4 by EB1-gold analysed by TIRF microscopy. Representative kymographs are shown. Microtubules were grown in the presence of rhodamine-labelled GMPCPP-tubulin seeds (red) and GFP-CLIP170-GCN4 (green). Fluorescent comets were observed in the presence of EB1-gold (top panel) or EB1 alone (middle panel), but were absent when the mix containing EB1-gold was ultracentrifuged before assembly (bottom panel, EB1-gold + spin). (**b**) TIRF microscopy of microtubules assembled in the presence of mCherry-EB1-gold (top-left panel), mCherry-EB1 (top-right panel), and when the mix containing mCherry-EB1-gold was ultracentrifuged before assembly (bottom panel). Scale bars in **a** and **b**: horizontal, 2 μm; vertical, 60 s. (**c**) CET of GTPγS-microtubules nucleated by isolated centrosomes in the presence of EB1-gold (Supplementary Table 2a). (**d**) CET of GDP-BeF_3^--microtubules nucleated by isolated centrosomes in the presence of EB1-gold (Supplementary Table 2b). (**e**) CET of GDP/Taxol microtubules assembled in the presence of EB1-gold (Supplementary Table 2c). (**f**) CET of GMPCPP-microtubules assembled in the presence of EB1-gold (Supplementary Table 2d). The EB1-gold concentration was 200 nM for all conditions. Each figure shows a projection of a few slices in the centre of the tomogram (top) and cross-sections also averaged over a few slices (bottom) corresponding to the boxed region in the upper image. Scale bars, 100 nm.

washing of the NPs, demonstrating the specificity of the Ni-trisNTA-6xHis interaction.

To test the functionality of EB1-gold, we analysed its ability to recruit binding partners to growing microtubule ends using total internal reflection fluorescence (TIRF) microscopy[14]. EB1-gold induced comet-like accumulations of two GFP-tagged protein variants, a dimeric version of the CAP-Gly domain-containing region of CLIP170 (GFP-CLIP170-GCN4, Fig. 1a), and a kinesin-1 motor protein fused to an EB1-interacting, SxIP motif-containing polypeptide chain fragment[15] (Kinesin-1-SxIP-GFP, Supplementary Fig. 1e). Centrifugation of the reaction mix to remove EB1-gold molecules abolished the formation of comets by the GFP-tagged proteins, demonstrating that these comets were not formed by EB1-HisLoop molecules released from NPs (Fig. 1a, bottom panel). To assess the microtubule tip tracking activity of EB1-gold in the absence of partner proteins, we produced a mCherry-EB1-HisLoop molecule that was conjugated to gold nanoparticles (mCherry-EB1-gold, Fig. 1b). mCherry-EB1-gold efficiently tracked growing microtubule ends, demonstrating further the functionality of the EB1-gold conjugate.

Since EB1 and its yeast orthologue Mal3 have been shown to interact with high affinity with microtubules assembled in the presence of GTPγS or GDP-BeF_3^-, but less well in the presence of GMPCPP[1,2],

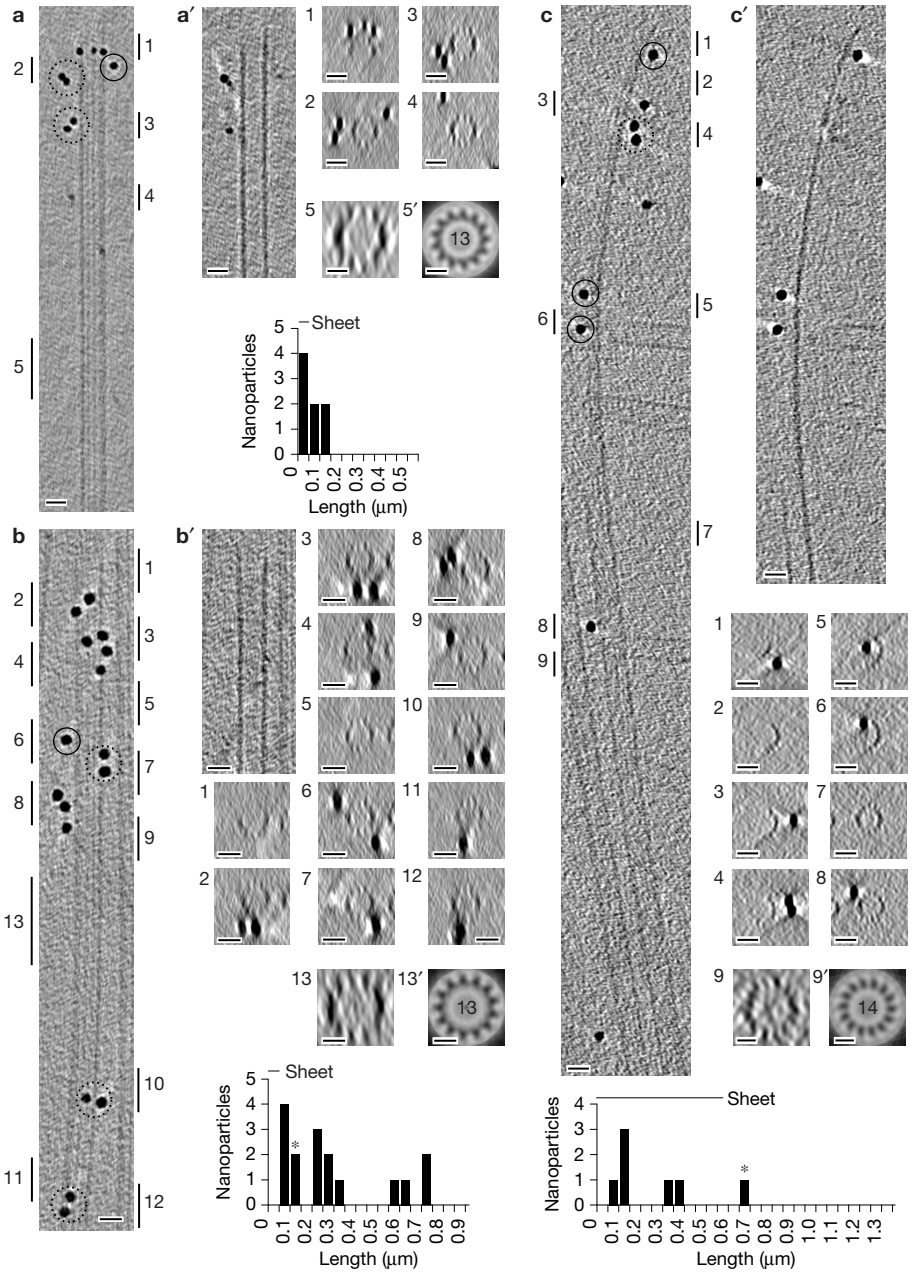

Figure 2 EB1-gold interacts with the outer surface of tubulin sheets and closed microtubule lattices. (**a**,**a′**) NPs of 6.5 nm average diameter at the end of a microtubule (Supplementary Table 2e). (**b**,**b′**,**c**,**c′**) NPs of 9.8 nm average diameter at the ends of microtubules with short (**b**, **b′**) and long (**c**, **c′**) sheet extensions (Supplementary Table 2g). The EB1-gold concentration was 94 nM and 22.5 nM with 6.5 nm and 9.8 nm NPs, respectively. Each panel comprises a projection along the *Z* direction that encompasses the microtubule and the NPs (**a**–**c**), *Z* projections of a few slices at the middle of the microtubule that highlight the shape of the tip (**a′**, **b′**, **c′**), and cross-sections along the microtubule axis that reveal the organization of the NPs around the lattice (**a**1–4, **b**1–12, **c**1–8). Vertical bars on each side of views **a**–**c** indicate the sub-regions used to produce the corresponding cross-sections. The protofilament number, *N*, was determined on cross-sections of complete microtubule lattices (**a**5, **b**13, **c**9), and was confirmed using *N*-fold rotational averaging (**a**5′, **b**13′, **c**9′). Dotted circles surround pairs of NPs, and plain circles surround NP singlets. The histograms show the distribution of NPs from the tip up to the least visible portion of the microtubules in the tomograms. Data were binned every 50 nm. The horizontal bar above the histograms indicates the portion of the lattice organized as sheets, and the asterisks correspond to NPs in interaction with both the microtubule lattice and the air/water interfaces. These NPs were discarded from the statistical analysis. Scale bars, 20 nm, except in **a**5,5′, **b**13,13′, **c**9,9′ where they represent 10 nm.

we assessed whether EB1-gold interacts with microtubules assembled in the presence of these GTP/GDP-P_i analogues. To this end, microtubules were nucleated from purified KE-37 centrosomes in the presence of GTPγS or GDP-BeF_3^-, while they were self-assembled in the presence of GMPCPP or Taxol. We found that EB1-gold at the maximal reachable concentration of 200 nM interacted strongly with GTPγS- and GDP-BeF_3^--microtubules (Fig. 1c,d, respectively). Control experiments in the presence of non-functionalized NPs

demonstrated that these were not trapped into the dense array of microtubules emanating from centrosomes (Supplementary Fig. 2a). Conversely, EB1-gold did not bind to microtubules assembled in the presence of Taxol or GMPCPP (Fig. 1e,f, respectively), in agreement with previous reports[1,2].

To localize EB1-gold at microtubule growing ends, they were nucleated from GMPCPP seeds in the presence of GTP (Fig. 2). Specimens were prepared in the presence of either 6.5 or 9.8 nm EB1-gold, and were vitrified ~3 min after the beginning of the tubulin polymerization process. In the former case, we added 10-nm-diameter gold NPs coated with anionic BSA as fiducial markers to facilitate automatic tracking of images during their acquisition[16]. However, we could not always differentiate EB1-gold from fiducial markers in these samples as a consequence of the large size distribution of the 6.5 nm NPs (Supplementary Fig. 1b). By contrast, due to their larger dimensions, the 9.8 nm EB1-gold conjugates could be directly used to register images by cross-correlation during the acquisition of tilt series. Hence, most of the data presented here were recorded on specimens prepared uniquely in the presence of 9.8 nm NPs conjugated to EB1-HisLoop, using final concentrations of 22.5 nM EB1-gold and 20 μM tubulin. Most of the tomograms used in this study were acquired in ice layers between ~50 and ~350 nm in thickness to limit nonspecific interactions of microtubules with the air/water interfaces (Supplementary Fig. 2b). In addition, only NPs close to microtubules and away from ice surfaces were taken into account.

Each panel of Fig. 2 shows a projection of a sub-tomogram along the *Z* axis that incorporates all NPs located around the tip of microtubules (Fig. 2a–c); a *Z* average of a few slices in their middle that highlights the shape of their extremity (Fig. 2a′, b′ and c′); and cross-sections, also averaged over a few slices, which reveal the organization of the NPs around the microtubules as well as the structure of their ends (sub-regions marked by numbers, identified as vertical bars in Fig. 2a–c). In most cases, the protofilament number of closed microtubules could be determined on *Z* projections by examining the specific fringe pattern of the superimposed protofilaments[17]; this value could be further confirmed on small projections along the microtubule axis and with the help of rotational averaging (cross-sections 5–5', 13–13', and 9–9' in Fig. 2a–c, respectively). Most microtubules with NPs attached to their extremities had 13 protofilaments (Supplementary Fig. 2c), consistent with a preferential interaction of EBs with this type of microtubule lattice[1,4,18].

The distribution of NPs was determined by measuring the distance of each NP from the tip of the microtubules (Fig. 2 and Supplementary Fig. 3). Among the total of 270 NPs observed at the ends of 33 microtubule extremities, 28 NPs were discarded as they were also found to interact with the air/water interfaces (Supplementary Table 1). The 242 remaining NPs were observed inside the ice layers, and thus were considered as true EB1-mediated interactions with microtubules. Within this population, 66 were organized as pairs (dotted circles in Fig. 2) with a centre-to-centre distance of 17.4 ± 3.2 nm, and 45 as singlets (plain circles in Fig. 2). The presence of two EB1-gold molecule populations was further confirmed by size-exclusion chromatography (Supplementary Fig. 2d). We could not find a preferred orientation of NP pairs with respect to the microtubule longitudinal axis, most likely as a consequence of the flexibility of the linker region between the amino- and C-terminal domains of EB1. The remaining NPs were

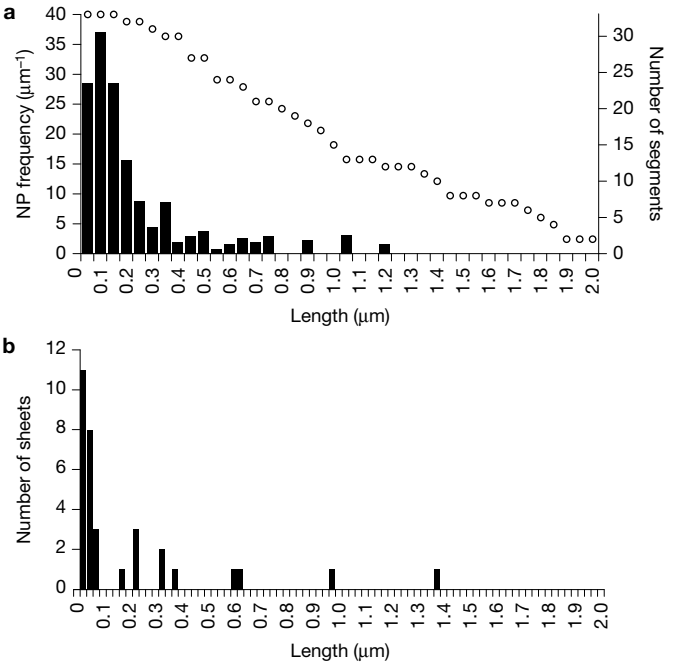

Figure 3 EB1-gold comets start from the tip of sheet structures and extend into closed regions of the microtubule lattice. (**a**) Average distribution of 9.8 nm EB1-gold at microtubule ends. The distances of NPs from microtubule tips were recorded on 33 extremities (statistical data are provided in Supplementary Table 1). Data were binned every 50 nm, and the NP frequency was determined for each 50 nm segment. The open circles indicate the number of segments included in each bin. (**b**) Sheet length distribution determined from the 33 microtubules analysed in **a**. Data were binned every 25 nm.

too closely packed to determine whether they were organized as pairs or singlets (see, for example, NP clusters at the tips of microtubules a–c in Supplementary Fig. 3A). Nevertheless, using the percentage of NPs organized as pairs or singlets and observed outside NP clusters, we can estimate that ~71.2% of the EB1-HisLoop monomers were conjugated to NPs. Related to the whole NP population, this gives an average of 5.2 EB1-HisLoop dimers attached at the ends of the 33 microtubules analysed in this study, with a maximum of ~11 EB1-HisLoop dimers (16 NPs) for the most dense NP comet (Supplementary Fig. 3Aa).

A large majority of NPs were observed facing the outside surface of sheets and closed microtubule regions (Supplementary Table 1), with a centre-to-centre distance between protofilaments and NPs of 16.6 ± 3.7 nm. NPs located close to sheet edges or facing their inside surface were occasionally observed (see, for example, sub-regions 5 and 6 in Fig. 2c), but represented only 2.1% of the total number of interaction events. NPs fully trapped inside microtubules were rarely observed (Supplementary Fig. 2e); however, such cases were also found in the presence of non-functionalized NPs. The mechanism by which EBs target growing microtubule ends has led to several hypotheses, including recognition of the lattice seam[19] and tubulin sheet edges[18]. While our results do not support these previous models, they are compatible with and extend cryo-electron microscopy-based observations that showed that EBs bind between two protofilaments at the corner of four tubulin dimers[2,4].

The distribution of NPs was highly variable, sometimes starting from the most distal extremity of microtubules (Supplementary

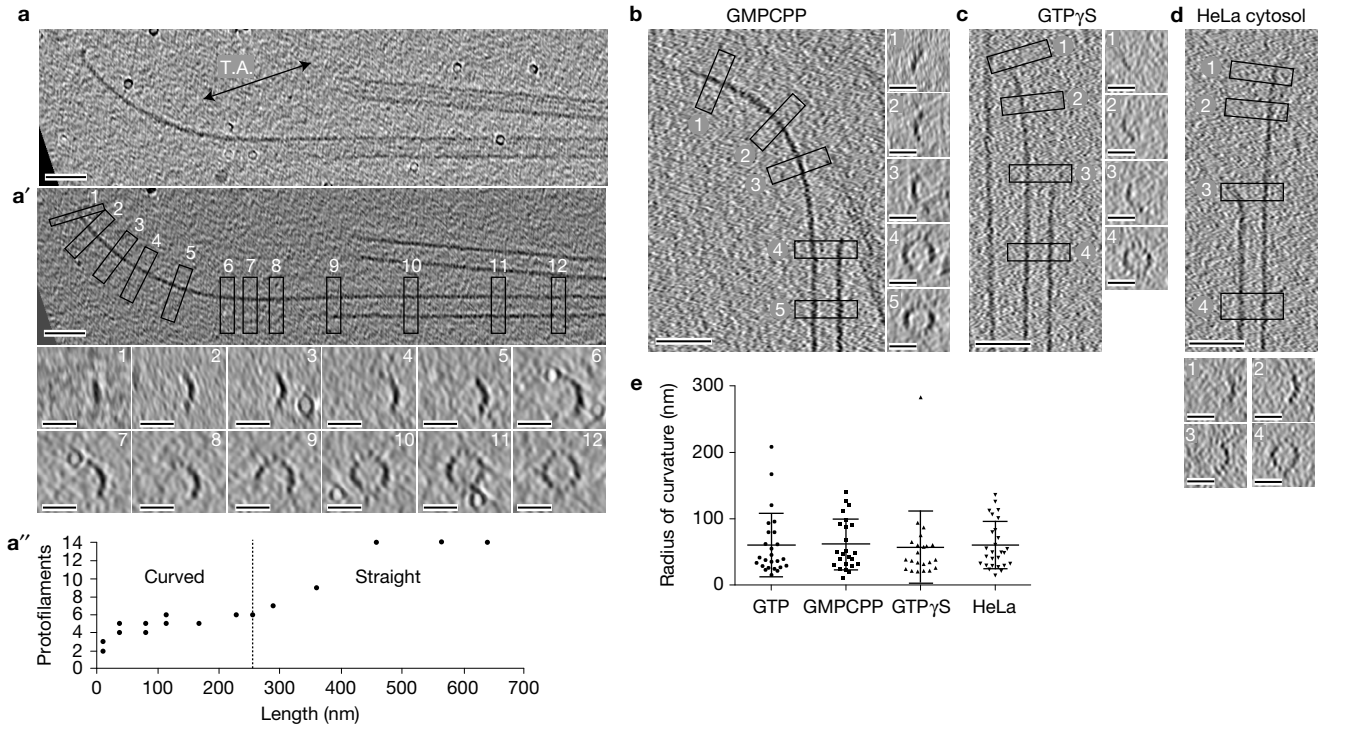

Figure 4 Tubulin sheets at the ends of growing microtubules display outward curvature independently of the nucleotide state of tubulin or when assembled in HeLa cell extracts. (**a**) *Z* projection of a microtubule extremity. T.A., tilt axis. NPs were erased before 3D reconstruction and appear as white spheres surrounded by a black halo. (**a′**) *Z* projection of a few slices in the middle of the microtubule in **a**. Boxes indicate regions extracted along the length of the microtubule to produce the cross-sections numbered from 1 to 12. (**a″**) Protofilament number from the tip to the microtubule body. The number of protofilaments was determined on the cross-sections 1–12 in **a′**. The sheet structure elongates along the *Z* direction when it orients towards the perpendicular of the tilt axis[33]. Hence, two values are provided for sections 1–4 where the protofilament number could not be accurately determined. The vertical dotted line in the graph delimitates approximately the longitudinally curved and straight regions of the lattice. Scale bars for **a**,**a′**, 50 nm; cross-sections, 25 nm. (**b**) Extremity of a GMPCPP-microtubule (see also Supplementary Fig. 4a–e and Supplementary Table 2i). (**c**) Extremity of a GTPγS-microtubule (see also Supplementary Fig. 4f–k and Supplementary Table 2j). (**d**) Extremity of a microtubule assembled in high-speed supernatants of HeLa cell extracts (see also Supplementary Fig. 5 and Supplementary Table 2k). In each panel **b**–**d**, a *Z* projection of a few slices in the middle of the microtubules is shown (**b**,**c**, left; **d**, top), as well as cross-sections (**b**,**c**, right; **d**, bottom) corresponding to the boxed regions numbered on the *Z* projections. Scale bars in **b**–**d**: *Z* projections, 50 nm; cross-sections, 25 nm. (**e**) Sheet curvature in the presence of different nucleotides and in cell extracts. Scattered plot of individual data with the mean (long horizontal bar) and standard deviation (short horizontal bars) displayed for each data set. $n = 24, 24, 22, 27$ microtubule ends for the GTP, GMPCPP, GTPγS and HeLa cell extracts, respectively. Statistical comparison in sheet curvature between the different conditions did not reveal any significant differences ($P > 0.05$, see Supplementary Table 3).

Fig. 3Ab,c and f), or away from the tip by a few tens of nanometres (Fig. 2a–c and Supplementary Fig. 3Aa,d,e,g–i). To obtain an overall view of the distribution of NPs at microtubule ends, we averaged individual distributions (Fig. 3a). This gave rise to a comet-like NP distribution with a maximum offset of ∼50–100 nm from the distal microtubule tip, which decreased rapidly after ∼350 nm and vanished after ∼1 μm. Superposition of this distribution with that of tubulin sheets present at microtubule ends (Fig. 3b) shows that the lower binding of EB1-gold to distal ends coincides with the presence of sheet structures. A recent high-resolution fluorescence microscopy study of EB comet size and location at growing microtubules ends suggested the presence of an EB-excluding region at the distal tip of microtubules[20]. While our data did not reveal such an excluding region, we note that we worked at an EB1-gold concentration (22.5 nM) supposed to induce a short excluding region according to this previous study. Furthermore, our 10 nm gold probe attached some 17 nm away from the microtubule lattice might not have provided sufficient precision to reveal such a feature. To obtain a better comparison between the respective NP frequencies at the outer surface of open tubulin sheets and closed microtubule lattices, we focused on the first 150 nm from the distal tip where the two types of structure coexist. NP frequencies of $19.8 \pm 30.7\ \mu m^{-1}$ and $43.4 \pm 19.1\ \mu m^{-1}$ for sheets and closed microtubules were measured, respectively (Supplementary Table 1). However, this difference might not be significant since elongating sheets contain necessarily less EB1-binding sites than closed microtubule lattices. Higher resolution data will be required to address this issue in more detail.

We found that EB1-gold molecules localize to the outer surface of closed microtubules, as well as to that of straight and outwardly curved sheet structures. Analysis of local averages along sheet extensions confirms that they are composed of closely juxtaposed protofilaments[21] (Fig. 4a, a′). Sheet structures are curved below 5 to 7 protofilaments (Fig. 4a″) and become straight above this range. This change in curvature with respect to protofilament number was previously modelled using the assumption that protofilaments have an intrinsic longitudinal curvature similar to that of GDP-tubulin rings[22]. Since recent studies suggest that EBs target the GTP-cap of growing microtubule ends[1–3,5,6], curved sheets may indeed be composed of

intrinsically curved GTP- and/or GDP-P_i-liganded tubulin dimers. To test this hypothesis, we analysed by CET the end structures of microtubules assembled without EB1-gold but in the presence of GMPCPP (Fig. 4b and Supplementary Fig. 4a–e) or GTPγS (Fig. 4c and Supplementary Fig. 4f–k). In both cases, growing microtubule ends displayed outwardly curved tubulin sheets similar to those observed at the tips of microtubules assembled in the presence of GTP. Since fluorescent EB1-GFP comets have been shown to extend over several tens to hundreds of nanometres in cells[6], we wanted to assess whether microtubules assembled in an environment close to cell conditions would also display curved tip structures. To this end, we prepared cytosolic HeLa cell extracts to which purified centrosomes were added to facilitate microtubule nucleation. Outwardly curved sheets were indeed observed under such conditions (Fig. 4d and Supplementary Fig. 5), indicating that microtubule assembly *in vitro* and in cells follow a similar mechanistic principle.

To address whether subtle differences in sheet curvature depend on the nucleotide state of tubulin, we measured the curvature of sheets in the first 50 nm from the distal tip of microtubules assembled in the presence of GTP, GMPCPP, GTPγS or cell extracts (Fig. 4e). Similar radii of curvature were found, with mean values in the range between 56–60 nm, values that are about three times higher than the averaged radius of curvature of GDP-tubulin rings[23]. Statistical comparison between the mean curvatures of sheets assembled in these different conditions did not reveal any significant differences (Supplementary Table 3). Since the conformation of a sheet depends on both the intrinsic curvature of the tubulin dimer and the number of protofilaments[22] (Fig. 4a–a″), a detailed structural analysis of sheet structures in these different assembly conditions will be required to assess whether the intrinsic curvature of tubulin varies with its nucleotide state[24,25].

Our data have implications for understanding the architecture of the GTP cap of growing microtubules (Fig. 5a,b). Our results suggest that the GTP-cap region incorporates both outwardly curved and straight regions of tubulin sheets, and extends into closed portions of the microtubule lattice. They are also consistent with GTP- and/or GDP-P_i-tubulin dimers present in the GTP-cap region. It is well established that GTP-tubulin adopts a curved conformation in solution[26–28], explaining why it assembles into outwardly curved sheets through a two-dimensional assembly process[21]. Tubulin dimers gradually straighten as the sheet widens, due to the increase in lateral curvature of the microtubule wall (F_{lat}) that counteracts the longitudinal curvature of the protofilaments[22] (F_{long}). GTP hydrolysis could happen soon after tubulin incorporation (Fig. 5b (1)), giving rise to a short layer of GTP-tubulin molecules at microtubule ends. However, the fact that EB1-binding sites include outwardly curved and straight regions of the microtubule lattice over several hundreds of nanometres (Fig. 5a) suggests that these regions must also be in a 'GTP-like' state, most probably in an intermediate GDP-P_i state[29], to which EBs display high affinity[2,4]. Alternatively, GTP hydrolysis could occur at some stage during the sheet straightening process (Fig. 5b (2)), or ultimately after full straightening of the tubulin dimers (Fig. 5b (3)). This latter hypothesis would agree with a recent description of the pre- and post-hydrolysis steps inside fully assembled microtubules[4,30]. Our model further postulates that by tethering outwardly curved tubulin dimers in elongating sheets, EBs may accelerate tubulin straightening

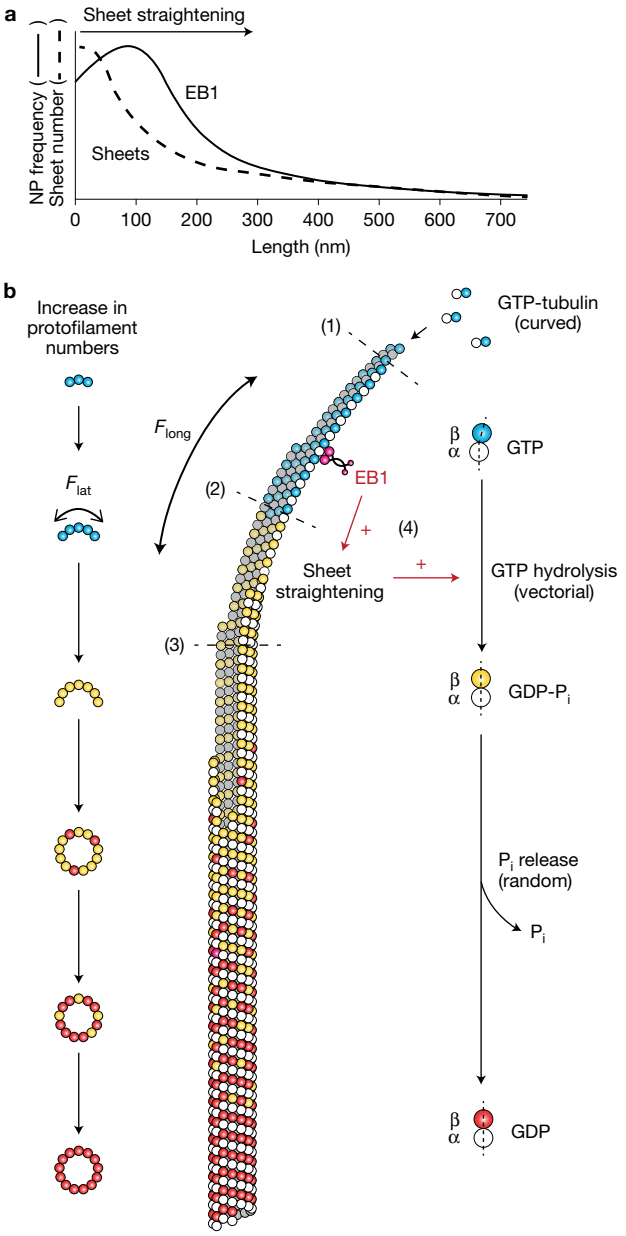

Figure 5 Mechanism of GTP/GDP-P_i-cap formation during microtubule growth. (**a**) Schematic distribution of EB1 (solid line) and sheets (dashed line), adapted from Fig. 3. The radial curvature of sheets increases from the tip to the microtubule body (arrow). (**b**) The different nucleotide states of tubulin are presented with the β-tubulin subunit in blue (GTP), yellow (GDP-P_i) and red (GDP). The region recognized by EB1 is supposed to comprise GTP- and GDP-P_i-tubulin molecules. GTP-tubulin is intrinsically curved in solution and assembles into outwardly curved sheets that gradually straighten as their protofilament number increases, due to the conflicting lateral (F_{lat}) and longitudinal (F_{long}) forces present in the microtubule lattice. GTP hydrolysis occurs through a vectorial process that follows the gradual straightening of the sheet structure, giving rise to GDP-P_i lattices and GDP lattices after random release of the γ-phosphate (P_i). Three alternative hypotheses are presented: (1) immediate hydrolysis after tubulin addition at growing microtubule ends, (2) hydrolysis during the straightening process, and (3) hydrolysis after full straightening of the protofilaments. The dashed lines delineate the GTP/GDP-P_i transition in these three situations. EB1 is proposed to promote sheet straightening (4), and thus GTP hydrolysis (red arrows with a plus sign). The microtubule in Fig. 4a,a′ was used as a template to schematically represent the microtubule in three dimensions (middle part) and its cross-sections (left part).

and hence GTP hydrolysis[4], accounting for its sheet closure activity[18] and its reduction of comet size at increasing concentrations[1,20,31] (Fig. 5b (4)). We note that while differing in the details, our alternative proposals for the linking between tubulin conformational changes and GTP hydrolysis (Fig. 5b (1–3)) share a common mixed coupled hydrolysis/random phosphate release mechanism[32]. In conclusion, our results provide a solid framework for further structural and modelling studies aimed at addressing the intimate relationship between tubulin conformational changes and GTP hydrolysis during microtubule assembly. □

METHODS

Methods, including statements of data availability and any associated accession codes and references, are available in the online version of this paper.

Note: Supplementary Information is available in the online version of the paper

ACKNOWLEDGEMENTS

We thank F. Percevault and C. Brigand for their help with cell cultures, and M.F. Carlier for her advice on BeF_3^- experiments. D.C. was supported by grants from the French National Agency for Research (ANR PCV06_142769 and PCV07_190830), the University of Rennes 1 (Emerging Scientific Challenges 2011–12), the Federative Research Institute Biosit (Innovative Scientific Project 2012), and the Association for Cancer Research (Blank Program 2011–15). A.A. was supported by a grant from the Netherlands Organization for Scientific Research Aard-en-Levenswetenschapen VICI. M.O.S. was supported by grants from the Swiss National Science Foundation (310030B_138659 and 31003A_166608). R.T. was supported by the German Research Foundation (Cluster of Excellence-Macromolecular Complexes, SFB807 and SPP1623). A.G. was the recipient of a PhD fellowship from the French Ministry of Education and Research. F.B. was the recipient of a post-doctoral fellowship from the French Association for Cancer Research (ARC). R.M.B. was the recipient of a contract from the 'Ramón y Cajal' programme of the Spanish Ministry of Economy and Competitivity, and was supported by a Marie Curie Career Integration Grant (EB-SxIP; FP7-PEOPLE-2011-CIG-293831). R.M. was the recipient of a European Molecular Biology Organization Long-Term Fellowship and Marie Curie International Incoming Fellowship. R.R.G. was the recipient of a European Molecular Biology Organization Long-Term Fellowship.

AUTHOR CONTRIBUTIONS

A.G. performed the microtubule EB1-gold experiments, and recorded and reconstructed cryo-electron tomograms. F.B. recorded cryo-electron tomograms on the EB1-gold samples and performed the GMPCPP, GTPγS, GDP-BeF_3^- and Taxol experiments. R.M.B. and M.O.S. designed the recombinant EB1-HisLoop proteins, and participated in the design of the project in close collaboration with D.C. R.M., R.R.G. and A.A. planned and performed the TIRF experiments. S.M. performed the HeLa cytosol experiments. M.A. and C.H. were involved in the purification of the recombinant EB1-HisLoop protein, tubulin and centrosomes. R.T. and R.W. prepared the Ni-trisNTA, and L.D. the functionalized mix-Capped NPs. D.C. and M.O.S. supervised the work and wrote the manuscript with the contributions from all authors.

COMPETING FINANCIAL INTERESTS

The authors declare no competing financial interests.

Published online at http://dx.doi.org/10.1038/ncb3412
Reprints and permissions information is available online at www.nature.com/reprints

1. Maurer, S. P., Bieling, P., Cope, J., Hoenger, A. & Surrey, T. GTPγS microtubules mimic the growing microtubule end structure recognized by end-binding proteins (EBs). *Proc. Natl Acad. Sci. USA* **108,** 3988–3993 (2011).
2. Maurer, S. P., Fourniol, F. J., Bohner, G., Moores, C. A. & Surrey, T. EBs recognize a nucleotide-dependent structural cap at growing microtubule ends. *Cell* **149,** 371–382 (2012).
3. Zanic, M., Stear, J. H., Hyman, A. A. & Howard, J. EB1 recognizes the nucleotide state of tubulin in the microtubule lattice. *PloS ONE* **4,** e7585 (2009).
4. Zhang, R., Alushin, G. M., Brown, A. & Nogales, E. Mechanistic origin of microtubule dynamic instability and its modulation by EB proteins. *Cell* **162,** 849–859 (2015).
5. Akhmanova, A. & Steinmetz, M. O. Microtubule end binding: EBs sense the guanine nucleotide state. *Curr. Biol.* **21,** R283–R285 (2011).
6. Seetapun, D., Castle, B. T., McIntyre, A. J., Tran, P. T. & Odde, D. J. Estimating the microtubule GTP cap size *in vivo*. *Curr. Biol.* **22,** 1681–1687 (2012).
7. Hyams, J. S. & Lloyd, C. W. *Microtubules* (Wiley-Liss, 1994).
8. Mitchison, T. & Kirschner, M. Dynamic instability of microtubule growth. *Nature* **312,** 237–242 (1984).
9. Carlier, M. F., Hill, T. L. & Chen, Y. Interference of GTP hydrolysis in the mechanism of microtubule assembly: an experimental study. *Proc. Natl Acad. Sci. USA* **81,** 771–775 (1984).
10. Pantaloni, D. & Carlier, M. F. Involvement of guanosine triphosphate (GTP) hydrolysis in the mechanism of tubulin polymerization: regulation of microtubule dynamics at steady state by a GTP cap. *Ann. NY Acad. Sci.* **466,** 496–509 (1986).
11. Levy, R. *et al.* A generic approach to monofunctionalized protein-like gold nanoparticles based on immobilized metal ion affinity chromatography. *ChemBioChem* **7,** 592–594 (2006).
12. Duchesne, L., Gentili, D., Comes-Franchini, M. & Fernig, D. G. Robust ligand shells for biological applications of gold nanoparticles. *Langmuir* **24,** 13572–13580 (2008).
13. Tinazli, A. *et al.* High-affinity chelator thiols for switchable and oriented immobilization of histidine-tagged proteins: a generic platform for protein chip technologies. *Chemistry* **11,** 5249–5259 (2005).
14. Bieling, P. *et al.* Reconstitution of a microtubule plus-end tracking system *in vitro*. *Nature* **450,** 1100–1105 (2007).
15. Doodhi, H., Katrukha, E. A., Kapitein, L. C. & Akhmanova, A. Mechanical and geometrical constraints control kinesin-based microtubule guidance. *Curr. Biol.* **24,** 322–328 (2014).
16. Coquelle, F. M. *et al.* Cryo-electron tomography of microtubules assembled *in vitro* from purified components. *Methods Mol. Biol.* **777,** 193–208 (2011).
17. Chrétien, D. & Wade, R. H. New data on the microtubule surface lattice. *Biol. Cell.* **71,** 161–174 (1991).
18. Vitre, B. *et al.* EB1 regulates microtubule dynamics and tubulin sheet closure *in vitro*. *Nat. Cell. Biol.* **10,** 415–421 (2008).
19. Sandblad, L. *et al.* The *Schizosaccharomyces pombe* EB1 homolog Mal3p binds and stabilizes the microtubule lattice seam. *Cell* **127,** 1415–1424 (2006).
20. Maurer, S. P. *et al.* EB1 accelerates two conformational transitions important for microtubule maturation and dynamics. *Curr. Biol.* **24,** 372–384 (2014).
21. Chrétien, D., Fuller, S. D. & Karsenti, E. Structure of growing microtubule ends: two-dimensional sheets close into tubes at variable rates. *J. Cell Biol.* **129,** 1311–1328 (1995).
22. Jánosi, I. M., Chrétien, D. & Flyvbjerg, H. Modeling elastic properties of microtubule tips and walls. *Eur. Biophys. J.* **27,** 501–513 (1998).
23. Muller-Reichert, T., Chrétien, D., Severin, F. & Hyman, A. A. Structural changes at microtubule ends accompanying GTP hydrolysis: information from a slowly hydrolyzable analogue of GTP, guanylyl (α,β)methylenediphosphonate. *Proc. Natl Acad. Sci. USA* **95,** 3661–3666 (1998).
24. Hyman, A. A., Chrétien, D., Arnal, I. & Wade, R. H. Structural changes accompanying GTP hydrolysis in microtubules: information from a slowly hydrolyzable analogue guanylyl-(α,β)-methylene-diphosphonate. *J. Cell Biol.* **128,** 117–125 (1995).
25. Wang, H. W. & Nogales, E. Nucleotide-dependent bending flexibility of tubulin regulates microtubule assembly. *Nature* **435,** 911–915 (2005).
26. Buey, R. M., Diaz, J. F. & Andreu, J. M. The nucleotide switch of tubulin and microtubule assembly: a polymerization-driven structural change. *Biochemistry* **45,** 5933–5938 (2006).
27. Rice, L. M., Montabana, E. A. & Agard, D. A. The lattice as allosteric effector: structural studies of αβ- and γ-tubulin clarify the role of GTP in microtubule assembly. *Proc. Natl Acad. Sci. USA* **105,** 5378–5383 (2008).
28. Nawrotek, A., Knossow, M. & Gigant, B. The determinants that govern microtubule assembly from the atomic structure of GTP-tubulin. *J. Mol. Biol.* **412,** 35–42 (2011).
29. Melki, R., Carlier, M. F. & Pantaloni, D. Direct evidence for GTP and GDP-Pi intermediates in microtubule assembly. *Biochemistry* **29,** 8921–8932 (1990).
30. Alushin, G. M. High-resolution microtubule structures reveal the structural transitions in αβ-tubulin upon GTP hydrolysis. *Cell* **157,** 1117–1129 (2014).
31. Duellberg, C., Cade, N. I., Holmes, D. & Surrey, T. The size of the EB cap determines instantaneous microtubule stability. *Elife* **5,** e13470 (2016).
32. Bowne-Anderson, H., Zanic, M., Kauer, M. & Howard, J. Microtubule dynamic instability: a new model with coupled GTP hydrolysis and multistep catastrophe. *Bioessays* **35,** 452–461 (2013).
33. Guesdon, A., Blestel, S., Kervrann, C. & Chrétien, D. Single versus dual-axis cryo-electron tomography of microtubules assembled *in vitro*: limits and perspectives. *J. Struct. Biol.* **181,** 169–178 (2013).

METHODS

Cloning and purification of recombinant proteins. Human EB1 cDNA (GI: 6912494) was subcloned in the pET-3d vector (Novagen) and purified as described previously[34]. A 6xHis-tag (GAGS-HHHHHH-SSGA) was inserted between residues Glu232 and Gly233, resulting in a construct denoted EB1-HisLoop. mCherry-tagged EB1-HisLoop was constructed by inserting the EB1-HisLoop coding region into an *ad hoc* modified pET28a vector (Novagen). The resulting fusion protein (denoted mCherry-EB1-HisLoop) contains mCherry connected to the N terminus of the EB1-HisLoop coding region by a flexible linker (AQAGGSGGAGSGGEGAVDG).

EB1-HisLoop was overexpressed in *Escherichia coli* strain BL21 (DE3) and purified by immobilized metal affinity chromatography according to the manufacturer's instructions (TALON cobalt affinity resin, Clontech). Fractions containing the protein were loaded on a Sephadex G-25 medium column (PD-10 Desalting column, Amersham Biosciences), previously equilibrated with BRB80 supplemented with 50 mM KCl. Eluted fractions were frozen in liquid nitrogen and stored at −80 °C. Protein purity was analysed by SDS–PAGE (Supplementary Fig. 1c). mCherry-EB1-HisLoop was overexpressed in *E. coli* strain BL21 (DE3) and purified by IMAC according to the manufacturer's instructions (HiTrap Chelating columns, GE Healthcare). The eluted fractions were pooled, concentrated and loaded onto a Superdex S200 16/60 column (GE Healthcare) equilibrated in 20 mM Tris-HCl, 300 mM NaCl, pH 7.5. The protein-containing fractions were pooled, concentrated and snap-frozen into liquid nitrogen before storage at −80 °C.

The GFP-CLIP170-GCN4 clone in pET28a was obtained after sequentially replacing the coiled-coil domain of wild-type human CLIP170 transcript variant 2 (GI: 38044112; from residue Gly349 to Ala1339) by the much shorter one of GCN4[35], and fusing an EmGFP (with an N-terminal His-tag) to the N terminus of the construct. Protein overexpression and purification were performed as described above for EB1-HisLoop, using 20 mM Tris-HCl, 500 mM NaCl, pH 7.5 for equilibrating the Superdex S200 column. Production and purification of kinesin-1-SxIP-GFP were described previously[15].

Tubulin and centrosome purification. Tubulin was purified from porcine brain by two cycles of assembly–disassembly followed by phosphocellulose chromatography and a final cycle of assembly–disassembly in the absence of GTP[36], and was obtained in BRB80 (80 mM PIPES, 1 mM $MgCl_2$, 1 mM EGTA, pH 6.8 with KOH) at a final concentration of 60 mg ml^{-1}. Aliquots were snap-frozen in liquid nitrogen and stored at −80 °C until use.

Centrosomes were isolated from KE-37 lymphoblastic cells as described previously[37]. Centrosomes were obtained in 55% to 65% sucrose fractions, 10 mM K-PIPES, pH 7.2, 1 mM EDTA, 0.1% β-mercaptoethanol, 0.1% Triton X-100, at concentrations in the range of $1 \sim 4.10^8$ centrosomes ml^{-1}. The most concentrated fractions were used for CET experiments.

Preparation of HeLa cytosol. HeLa cells were grown to confluency in Dulbecco's modified Eagle medium (DMEM, GIBCO Life Technology) complemented with 10% fetal calf serum and 1% penicillin-streptomycin-fungizone. After trypsinization and washing in cold (Ca^{2+}, Mg^{2+})-free PBS, the HeLa cell pellet was weighed and resuspended in a minimal volume of 0.6 ml per gram of pellet in (Ca^{2+}, Mg^{2+})-free PBS, 2 mM EGTA. Cells were homogenized on ice using a tight pestle in a 7 ml Dounce glass homogenizer. Mammalian protease inhibitor cocktail (Sigma) was added before centrifugation at 2,000*g* for 10 min at 4 °C. The supernatant was collected and further centrifuged at 100,000*g* (TLA-120.2, Beckman) for 30 min at 4 °C, aliquoted, snap-frozen into liquid nitrogen and stored at −80 °C until use.

Determination of NP size distribution and concentration. Nanoparticles of 5 nm and 10 nm nominal size (BBInternational Ltd) were characterized by transmission electron microscopy to determine their effective size distributions. NPs were diluted in water and transferred into Beckman ultracentrifuge tubes (5 × 41 mm) into which a Plexiglas support was inserted[37]. Formvar-carbon-coated 400 mesh electron microscope grids were deposited at the surface of the Plexiglas, and tubes were centrifuged in a TLS-55 rotor (Beckman), 221,000*g*, 30 min, 20 °C, for the 5 nm NPs, and 100,000*g*, 30 min, 20 °C, for the 10 nm NPs. Grids were recovered and imaged by transmission electron microscopy (Tecnai G^2 T20 Sphera, FEI). Images were analysed using the 'analyse particle' plugin of the ImageJ software. Diameters D were extrapolated from the nanoparticle areas A assuming spherical objects, using the relationship $D = \mathrm{sqrt}\,(2\pi/A)$. NP concentration was determined by spectrophotometry at 520 nm, using $\varepsilon_{520} = \exp(3.32 \times \ln(D) + 10.81)$, where ε_{520} is the extinction coefficient at 520 nm of gold NPs, and D (in nm) is their diameter[38]. Applied to the NP size distributions (Supplementary Fig. 1b), values of $\varepsilon = 2.75 \times 10^7$ l mol^{-1} cm^{-1} for 6.5 nm NPs and $\varepsilon = 10.01 \times 10^7$ l mol^{-1} cm^{-1} for 9.8 nm NPs were found.

Preparation of hexahistidine-Sepharose resin (His-resin). Two hundred microlitres of a biotinylated peptide (biotin-GAAHHHHHH, Peptide and Protein Research, PPR Ltd) at 7.9 mM was added to 3 ml of Strep-Tactin Sepharose resin (IBA) equilibrated in PBS (∼2 ml packed bed volume). The reaction was left overnight at room temperature on a rotary mixer. Seven millilitres of PBS supplemented with 0.005% of Tween-20 (PBS-T) was added and the reaction was left at room temperature for two more hours. The resin was then poured into a 10 ml column and washed five times with 10 resin volumes of PBS-T and two times with 10 resin volumes of PBS, to remove any unbound peptide. The His-resin was kept at 4 °C.

Preparation of the Ni-trisNTA mix-capped nanoparticles (Ni-trisNTA-NPs). CVVVT-ol peptidol was from Peptide and Protein Research (PPR Ltd), HS-PEG (HS-EC_{11}-EG_4, M_w 380) was from ProChimia (ProChimia Surfaces), and trisNTA-alkyl-OEG-thiol ligand (HS-C_{16}-EG_3-trisNTA; denoted trisNTA ligand) was synthesized according to published procedures[13]. Mix-capped nanoparticles (denoted NP_{nf}) consist of gold nanoparticles coated with a mixed matrix composed of CVVVT-ol and HS-PEG (CVVVT-ol:HS-PEG; 70:30) allowing their solubility and dispersion in physiological environments[12]. Addition of a Ni-trisNTA ligand at desired molar ratio within the Mix-matrix allows the specific attachment at controlled stoichiometry of the resulting Ni-trisNTA mix-capped nanoparticles to poly-histidine-tagged proteins[11]. Ni-trisNTA mix-capped nanoparticles (denoted Ni-trisNTA-NPs or NP_f) were prepared as previously described[12,39] with slight modifications: all buffers were supplemented with 0.005% Tween-20, nickel loading of the trisNTA ligand was performed using $NiCl_2$, all buffer exchanges were performed using G-25 size-exclusion chromatography and purification of the mix-capped nanoparticles bearing at least one Ni-trisNTA ligand per nanoparticle was performed using the home-made His-resin described above. When needed, NPs were concentrated by ultracentrifugation at room temperature, for 20 min at 40,000*g* and 80,000*g* for 9.8- and 6.5-nm-diameter nanoparticles, respectively.

EB1-nanoparticle conjugation. EB1-HisLoop or mCherry-EB1-HisLoop was mixed with 9.8 nm Ni-trisNTA-NPs (NP_f) at a 100:1 molar ratio. The mixture was incubated for between 1 and 2 h at 4 °C or room temperature under gentle stirring, centrifuged at 30,000*g*, 4 °C, 15 min (TLA-100, Beckman), and resuspended in PBS-T. Three additional centrifugation and resuspension cycles were performed to remove free EB1 molecules in suspension. EB1-gold was resuspended in BRB80 supplemented with 50 mM KCl after the last centrifugation step. Preparation of 6.5 nm NPs-EB1 conjugates was performed using the same procedure, except that centrifugation was carried out at 60,000*g*. For cryo-electron microscopy experiments, the EB1-NP conjugates were prepared extemporaneously and kept at 4 °C until use. For TIRF experiments, specimens were frozen in liquid nitrogen and kept at −80 °C until use. Their functionality was assessed by CET (Supplementary Table 2e), which revealed that freshly prepared EB1-NPs conjugates and frozen ones bound similarly to the tip of microtubules.

Determination of EB1-NP conjugation efficiency. The conjugation efficiency was determined by measuring the molar ratio between EB1-HisLoop monomers and NPs by SDS–PAGE analysis of the conjugates. Following conjugation of EB1-HisLoop with Ni-trisNTA-functionalized NPs (NP_f) and removal of excess protein by centrifugation as described above, the NP concentration was determined by spectrophotometry. Controls were performed in the presence of non-functionalized NPs (NP_{nf}). The final pellets, kept in a minimal volume of buffer, were resuspended into Laemmli loading buffer and a defined quantity (a few picomoles) was loaded onto a 12% polyacrylamide gel. Samples of EB1-HisLoop of known concentrations were loaded as concentration standards. The NPs did not penetrate the gel, which was further stained using Coomassie blue staining. The gel was digitized (U:Genius3, Syngene), and analysed using the ImageJ software. The quantity of EB1 monomers associated with the NPs was estimated with respect to the standards. The conjugation efficiency between EB1-HisLoop or mCherry-EB1-HisLoop and NPs was routinely verified by SDS–PAGE.

Size-exclusion chromatography of EB1-gold. The conjugates were analysed by size-exclusion chromatography using a Sephacryl S-300 high-resolution 1 × 18 cm column on a Biologic LP (Biorad) chromatography system. Four hundred microlitres of EB1-gold sample at a concentration of 9.8 nM was loaded on top of the column and eluted at a flow rate of 0.5 ml min^{-1} at room temperature. Recording was performed at 280 nm. Control experiments were performed with non-functionalized NPs (NP_{nf}) pre-incubated with EB1. The column was calibrated with 5, 10 and 15 nm gold NPs before running the experiment in the presence of EB1-gold and NP_{nf}.

Total internal reflection fluorescence microscopy. To reconstitute plus-end tracking *in vitro*, short microtubule seeds were prepared by incubating the tubulin mix containing 70% unlabelled porcine brain tubulin (Cytoskeleton), 17% biotin-tubulin (Cytoskeleton), 6% rhodamine-tubulin or Hilyte Fluor::tubulin (Cytoskeleton)

DOI: 10.1038/ncb3412

with 1 mM GMPCPP (Jena Biosciences) at 37 °C for 30 min. The polymers were depolymerized on ice for 30 min and repolymerized at 37 °C with 1 mM GMPCPP. The seeds were diluted tenfold in assay buffer (80 mM PIPES, 4 mM $MgCl_2$, 1 mM EGTA, pH adjusted to 6.8 with KOH) containing 10% glycerol, snap-frozen in liquid nitrogen and stored at −80 °C.

Flow chambers, assembled from cleaned glass coverslips and microscopic slides, were incubated first with 0.2 mg ml^{-1} PLL-PEG-biotin (Susos AG), washed with assay buffer, and then incubated with 1 mg ml^{-1} streptavidin. Immobilized seeds were attached to functionalized glass coverslips by biotin-neutravidin links. The flow chamber was further incubated with 1 mg ml^{-1} κ-casein to prevent nonspecific protein binding. The reaction mix (assay buffer supplemented with 15 μM porcine brain tubulin, 6 nM GFP-CLIP170-GCN4, 50 mM KCl, 1 mM GTP, 0.2 mg ml^{-1} κ-casein, 0.1% methylcellulose, and an oxygen scavenger composed of 50 mM glucose, 400 μg ml^{-1} glucose oxidase, 200 μg ml^{-1} catalase and 4 mM dithiothreitol) was spun in an airfuge for 5 min at 119,000*g* and added to the flow chamber. For the experiments with the Kinesin-1, we replaced the GFP-CLIP170-GCN4 in the reaction mixture by 10 nM of the kinesin-1-SxIP-GFP. EB1-HisLoop (100 nM) was centrifuged along with the reaction mix whereas EB1-gold (43.5 nM, conjugated to 6.5 nm diameter NPs) was added to the reaction mix after centrifugation. For control experiments, EB1-gold was added before centrifugation and was thus depleted from the suspension.

To perform the *in vitro* assay in the presence of fluorescent EB1, we substituted the EB1-HisLoop by mCherry-EB1-HisLoop (40 nM) and EB1-gold by mCherry-EB1-gold (40 nM, conjugated to 10-nm-diameter NPs). To visualize clearly growing microtubule events, we supplemented the reaction mix with 0.5 μM of fluorescent tubulin porcine HiLyte 488 (Cytoskeleton). mCherry-EB1-HisLoop was centrifuged along with the reaction mix and mCherry-EB1-gold was added after centrifugation. In control experiments mCherry-EB1-gold was added before spin down.

Microtubule specimens were observed at 30 °C using a TIRF microscope at 2 s per frame with 100 ms exposure time. TIRF microscopy was performed on an inverted research microscope Nikon Eclipse Ti-E (Nikon), equipped with the perfect focus system (Nikon), a TIRF-E motorized TIRF illuminator, with a CFI Apo TIRF 100 × 1.49 N.A. oil objective (Nikon), and with a QuantEM 512SC EMCCD camera (Roper Scientific) controlled by MetaMorph 7.5 software (Molecular Devices). To maintain the temperature at 30 °C, we used a stage top incubator (Tokai Hit) mounted on a motorized stage. For excitation, we used a 100 mW, 491 nm Calipso diode-pumped solid-state laser (Cobolt) and a 100 mW, 561 nm Jive diode-pumped solid-state laser (Cobolt) in combination with a Chroma ET-GFP/mCherry filter cube. Images were projected onto the CCD chip of a QuantEM camera with a Nikon C mount adapter 2.5X intermediate lens so that the final pixel size was 62 nm. Kymographs (length versus time plots) representing microtubule life history were made using MetaMorph and ImageJ software.

Preparation of microtubules in the presence of GTP/GDP-P_i analogues and Taxol at 200 nM EB1-gold concentration. Vitrification of specimens was performed using an automatic plunge freezer (EM GP, Leica) for the following experiments.

Microtubules in the presence of GTPγS were prepared by mixing in BRB80, 50 mM KCl, 5.5 μl of tubulin at 300 μM, 0.8 μl of GTPγS at 20 mM, 4 μl of KE-37 purified centrosomes, and 5 μl of EB1-gold (9.8 nm NP_f) or 9.8 nm NP_{nf} at 650 nM in a final volume of 16 μl to reach final concentrations of 100 μM tubulin, 1 mM of GTPγS and 200 nM of EB1-gold or NP_{nf}. This mixture was incubated at 35 °C in a test tube and 4 μl specimens were pipetted at specific times between 25 and 35 min, and were deposited on the electron microscope grid, followed by blotting and vitrification into liquid ethane (Supplementary Table 2a).

Microtubules in the presence of BeF_3^- were prepared by mixing in BRB80, 50 mM KCl, 3.2 μl of tubulin at 100 μM, 0.8 μl NaF at 200 mM, 0.8 μl $BeSO_4$ at 2 mM, 0.8 μl of GTP at 20 mM, 4 μl KE-37 purified centrosomes, and 5 μl of EB1-gold (9.8 nm NP_f) or 9.8 nm NP_{nf} at 650 nM in a final volume of 16 μl to reach final concentrations of 20 μM tubulin, 0.2 mM of BeF_3^- and 200 nM of EB1-gold or NP_{nf}. This mixture was incubated at 35 °C in a test tube and 4 μl specimens were pipetted at specific times between 7 and 13 min, and were deposited on the electron microscope grid, followed by blotting and vitrification into liquid ethane (Supplementary Table 2b).

Microtubules in the presence of Taxol were prepared by mixing in BRB80, 50 mM KCl, 4 μl of tubulin at 100 μM, 2 μl of GTP at 20 mM, 2 μl of paclitaxel at 400 μM in a final volume of 40 μl to reach final concentrations of 10 μM tubulin, 1 mM of GTP and 20 μM of Taxol. This sample was incubated at 35 °C during 24 h, then 11 μl was mixed with 5 μl of EB1-gold (9.8 nm NP_f) or 9.8 nm NP_{nf} at 650 nM to reach final concentrations of 200 nM EB1-gold or NP_{nf} . This mixture was incubated for 15 min at 35 °C and 4 μl was deposited on the electron microscope grid, followed by blotting and vitrification into liquid ethane (Supplementary Table 2c).

Microtubules in the presence of GMPCPP were prepared by mixing in BRB80, 50 mM KCl, 1.6 μl of tubulin at 100 μM, 1.6 μl of GMPCPP at 1 mM, and 5 μl of EB1-gold (9.8 nm NP_f) or 9.8 nm NP_{nf} at 650 nM in a final volume of 16 μl to reach final concentrations of 10 μM tubulin, 0.1 mM of GMPCPP and 200 nM of EB1-gold or NP_{nf}. This mixture was incubated at 35 °C in a test tube and 4 μl specimens were pipetted at specific times between 7 and 14 min, and were deposited on the electron microscope grid, followed by blotting and vitrification into liquid ethane (Supplementary Table 2d).

Preparation of microtubules in the presence of GTP and EB1-gold. Microtubule seeds were prepared extemporaneously by incubating tubulin at 3 μM in the presence of 0.1 mM GMPCPP in BRB80, 50 mM KCl, 4 min, 35 °C. Seeds were left at room temperature until use. Tubulin at 80 μM in BRB80, 100 mM KCl, 4 mM GTP was mixed at 4 °C with an equal volume of EB1-gold (9.8 nm) at 90 nM. One volume of this mixture was then added to one volume of GMPCPP-microtubule seeds, providing final concentrations of 20 μM tubulin in BRB80, 62.5 mM KCl, 1 mM GTP and 22.5 nM EB1-gold. Controls were prepared in the presence of non-functionalized NPs (NP_{nf}) using the same procedure (Supplementary Table 2g). Additional experiments in the presence of centrosomes at 10 μM tubulin concentration, 200 nM EB1-gold, 1 mM GTP were performed to confirm the specific interaction of EB1-gold with the plus-ends of growing microtubules (Supplementary Table 2h).

In the presence of 6.5 nm EB1-NPs, experiments were performed at 94 nM and 150 nM EB1-gold final concentrations, in the presence of 10 nm gold nanoparticles coated with anionic BSA (Aurion Gold Tracers, 210.122) prepared in BRB80, and used as fiducial markers during image acquisition and registration before 3D reconstruction[16]. Controls were performed at a final concentration of 150 nM NP_{nf} (6.5 nm, Supplementary Table 2e,f).

Specimens were incubated in a test tube at 35 °C and a 4 μl specimen was pipetted at specific times, between 2 and 4 min of assembly, and was deposited onto a holey-carbon grid held by tweezers in a humid and temperature-controlled atmosphere. Excess of the suspension was blotted using a filter paper, and the grid was quickly plunged into liquid ethane to vitrify the specimen.

Preparation of microtubules in the presence of GTP analogues and HeLa cytosol for the analysis of microtubule ends. During this study, we found that the mix-capped nanoparticles (NP_{nf}) could be conveniently used as fiducial markers, since their peptidol:PEG matrix has been optimized to avoid unspecific interactions with proteins[12]. Therefore, the following experiments were performed with NP_{nf} as fiducial markers.

Microtubules in the presence of GMPCPP were prepared by mixing in BRB80, 50 mM KCl, 4 μl of tubulin at 50 μM, 2 μl of GMPCPP at 1 mM, and 4 μl of EB1-gold (9.8 nm) at 650 nM, in a final volume of 20 μl to reach final concentrations of 10 μM tubulin, 0.1 mM of GMPCPP and 80 nM of fiducial NP_{nf}. This mixture was incubated at 35 °C in a test tube and 4 μl specimens were pipetted at specific times between 6 and 11 min, and were deposited on the electron microscope grid, followed by blotting and vitrification into liquid ethane (Supplementary Table 2i).

Microtubules in the presence of GTPγS were prepared by mixing in BRB80, 50 mM KCl, 10 μl of tubulin at 150 μM, 1 μl of GTPγS at 20 mM, 5 μl of KE-37 purified centrosomes, and 4 μl of 9.8 nm NP_{nf} at 400 nM, in a final volume of 20 μl to reach final concentrations of 75 μM tubulin, 1 mM of GTPγS and 80 nM NP_{nf}. This mixture was incubated at 35 °C in a test tube and 4 μl specimens were pipetted at specific times between 20 and 35 min, and were deposited on the electron microscope grid, followed by blotting and vitrification into liquid ethane (Supplementary Table 2j).

Microtubules in cell extracts were assembled by mixing 7 μl of HeLa cell cytosol with 2 μl of centrosomes and 150 nM of 9.8 nm NP_{nf} in a total volume of 10 μl. Four-microlitre specimens were incubated at 35 °C for periods of ∼2 min on the grid held by tweezers on the guillotine device under humidity and temperature control. Grids were blotted from behind to trap microtubule asters over the holes of the holey-carbon grid, followed by rapid freezing into liquid ethane (Supplementary Table 2k).

Cryo-electron tomography (CET). Grids were transferred to a single-axis cryo-holder (model 626, Gatan) and were observed using a 200 kV electron microscope (Tecnai G^2 T20 Sphera, FEI) equipped with a CCD camera. Two types of camera were used in this study, a 2 k × 2 k (USC1000, Gatan) and a 4 k × 4 k CCD camera (USC4000, Gatan). Single-axis tilt series, typically in the angular range ±60°, were acquired under low electron doses (∼0.3 $e^-/Å^2$) using the camera in binning mode 2 and at nominal magnifications of 25,000× or 29,000×. Tomograms were reconstructed using the graphical user interface eTomo from the IMOD software package[40]. Sub-tomograms containing individual microtubules were extracted using the graphical user interface 3dmod of the IMOD package. The microtubules were reoriented before extraction so that their long axis was parallel and perpendicular to the *Y* and *Z* axes of the sub-tomogram volumes, respectively. Measurements such as microtubule and sheet lengths, angular

orientations of the NP pairs with respect to the microtubule longitudinal axis, distances of the NPs from the microtubule lattice and the separation between NPs in pairs, were performed using the measuring tools available in the slicer panel of 3dmod. Rotational averaging of microtubule cross-sections was performed using a dedicated script written in ImageJ software. Curvature measurements were performed in the first 50 nm from the sheet extremities, using the '3-point' method described at: http://www.intmath.com/applications-differentiation/8-radius-curvature.php.

Cell lines. No cell lines used in this study were found in the database of commonly misidentified cell lines that is maintained by ICLAC and NCBI Biosample. The HeLa cell line used to prepare cytosolic extracts was taken from stocks maintained by the cell culture service of the IGDR. This cell line was not authenticated. HeLa cells were treated by BM-Cyclin (Roche) and were tested negative for mycoplasma. KE-37 cells were purchased from DSMZ, cell line no. ACC 46. According to DSMZ, KE-37 cells were authenticated by multiplex PCR of minisatellite markers. They were treated with Baytril and tested negative for mycoplasma.

Statistics and reproducibility. TIRF experiments in the presence of EB1-gold and GFP-CLIP170-GNC4 (Fig. 1a), EB1-gold and kinesin-1-SxIP-GFP (Supplementary Fig. 1d), and mCherry-EB1-gold (Supplementary Fig. 1b) were repeated at least two times. CET experiments with EB1-gold were typically performed in parallel with controls in the presence of non-functionalized NPs prepared the same day under similar conditions. At least three grids were prepared for each experimental condition examined in this study. The complete study incorporated 262 tomograms (see Supplementary Table 2 for details). Protein purity and conjugation efficiency were routinely verified by SDS–PAGE.

Statistical comparison between the sheet curvature of microtubules assembled in the presence of different nucleotides and in HeLa cell extracts was performed using a Kruskal–Wallis test followed by Dunn's multiple comparisons test (see Supplementary Table 3 for details).

Data availability. Sub-tomograms were deposited in the Electron Microscopy Data Bank (EMDB) with the primary accession codes: EMD-2912 (Fig. 2a–a′), EMD-2915 (Fig. 2b–b′), EMD-2916 (Fig. 2c–c′), EMD-2918 (Fig. 4a–a′), EMD-2919 (Fig. 4b), EMD-2920 (Fig. 4c) and EMD-2921 (Fig. 4d). All other data supporting the findings of this study are available from the corresponding author on request.

34. Buey, R. M. *et al.* Insights into EB1 structure and the role of its C-terminal domain for discriminating microtubule tips from the lattice. *Mol. Biol. Cell* **22,** 2912–2923 (2011).
35. O'Shea, E. K., Klemm, J. D., Kim, P. S. & Alber, T. X-ray structure of the GCN4 leucine zipper, a two-stranded, parallel coiled coil. *Science* **254,** 539–544 (1991).
36. Ashford, A. J., Anderson, S. S. L. & Hyman, A. A. in *Cell Biology: A Laboratory Handbook* 2nd edn, Vol 2 (ed. Celis J. E.) 205–212 (Academic, 1998).
37. Chrétien, D., Buendia, B., Fuller, S. D. & Karsenti, E. Reconstruction of the centrosome cycle from cryoelectron micrographs. *J. Struct. Biol.* **120,** 117–133 (1997).
38. Liu, X., Atwater, M., Wang, J. & Huo, Q. Extinction coefficient of gold nanoparticles with different sizes and different capping ligands. *Colloids Surf. B.* **58,** 3–7 (2007).
39. Duchesne, L. *et al.* Transport of fibroblast growth factor 2 in the pericellular matrix is controlled by the spatial distribution of its binding sites in heparan sulfate. *PLoS Biol.* **10,** e1001361 (2012).
40. Mastronarde, D. N. Dual-axis tomography: an approach with alignment methods that preserve resolution. *J. Struct. Biol.* **120,** 343–352 (1997).